Influence of Scattered Radiation on the Efficiency of Dual High-Energy X-Ray Imaging for Material Characterization

Sanjeevareddy KOLKOORI, Gerd-Rüdiger JAENISCH, Andreas DERESCH
Bundesanstalt für Materialforschung und -prüfung (BAM), Berlin, Germany

Gerd-Ruediger.Jaenisch@bam.de

Abstract. In this contribution, we discuss the influence of scattered radiation on materials' effective attenuation coefficients at higher X-ray energies. The selected X-ray spectra for the dual-energy experiments correspond to 3 MV and 7.5 MV acceleration potential of the used betatron. Experiments were performed on a test phantom containing step wedges of different low- and high-Z materials. We evaluated the ratio between low- and high-energy X-ray attenuation coefficients quantitatively based on simulated poly-energetic high-energy X-ray source spectra and the detector sensitivity using the "analytical Radiographic Testing inspection simulation tool" (*aRTist*) developed at BAM. Furthermore, the influence of scattered radiation is evaluated using an efficient Monte-Carlo simulation. The simulation results are compared quantitatively with experimental investigations. Finally, important applications of the proposed technique in the context of aviation security are discussed.

1 Introduction

Conventional dual energy (<450 keV) X-ray imaging is a well-established technique in the medical field and for baggage screening applications at airports [1-3]. Generally, medical dual-energy systems and baggage scanners operate with acceleration potentials between 80 kV and 160 kV. The corresponding X-ray spectra are well separated, resulting in the dominance of either the photoelectric absorption or the Compton effect for many materials. In addition, for typical applications the effective mass attenuation coefficient is strongly dependent on the atomic number Z. This leads to lower complexity in material discrimination by using the dual-energy function, which describes the ratio between low- and high-energy X-ray attenuation coefficients. In the case of large air-cargo container inspection the radiation beam penetrates several meters, resulting in a strong dependence of the effective attenuation coefficient μ_{eff} on the material thickness. Furthermore, due to the decreased separation between high-energy (>1 MeV) X-ray spectra, μ_{eff} is less dependent on Z, but shows strong dependence on the material density variations.

Compared to conventional X-ray imaging, high-energy digital radiography (DR) is required for the NDT of densely packed steel or aluminium containers because of the high penetration power when applied to thick objects. The ability to distinguish between low- and high-Z materials is then based on the balance between the Compton effect and pair production. For this purpose, industrial NDT high-energy X-ray sources are available, such

as linear accelerators (linac) [4] and portable X-ray betatrons [5,6], which are suitable for the inspection of large objects. The reason for selecting an X-ray betatron as high-energy radiation source for our present investigations is due to its ability to penetrate 350 mm of steel or 1.5 m of heterogeneous concrete structures. Additionally, due to the comparatively small size of its focal spot (1.5×3 mm^2, derived from measurements), the digital image quality can be significantly improved in terms of the spatial resolution of an image. Furthermore, no special cooling systems are necessary, making it highly suitable for mobile NDT applications. Recent investigations with high-resolution Digital Detector Arrays (DDAs) have shown the improvement of essential image quality parameters such as image basic spatial resolution (SR_b) and contrast-noise-ratio (CNR) when compared to computed radiography (CR) [7,8]. These main advantages are considered in the presented experimental technique.

The aim of this paper is threefold. First, the general analytical solution for evaluating dual high-energy X-ray images using the continuous-spectrum X-ray attenuation method is discussed. Then, numerical results for the dependence of the dual-energy function on the material thickness and the scattered radiation contribution are presented. Following, experimental and simulated dual-energy images of a test phantom containing different low- and high-Z step wedges are compared. Finally, important applications of the proposed technique in the context of aviation security are discussed.

2 Dual High-Energy X-ray Imaging

2.1 Without Scattered Radiation

The energy dependent incident and transmitted X-ray intensities for a homogeneous object illuminated by a poly-energetic X-ray beam are expressed in terms of the X-ray source spectrum $S(E)$ and the detector sensitivity $D(E)$:

$$\text{Incident intensity: } I_0 = \int_{E=0}^{E_{\max}} S(E)\cdot D(E)\,dE\,, \tag{1}$$

$$\text{Transmitted Intensity: } I = \int_{E=0}^{E_{\max}} S(E)\cdot D(E)\,\mathrm{e}^{-\mu(\mathrm{E})\cdot \mathrm{t}}\,dE\,. \tag{2}$$

The effective linear attenuation coefficient is derived using the Beer-Lambert law as described in [9,10]

$$\begin{aligned}\mu_{eff} &= \frac{1}{t}\left(-\log\left(\frac{I}{I_0}\right)\right) = \frac{1}{t}\left(-\log\left(\frac{\int_{E=0}^{E_{\max}} S(E)\cdot D(E)\ \mathrm{e}^{-\mu(\mathrm{E})\cdot \mathrm{t}}\,dE}{\int_{E=0}^{E_{\max}} S(E)\cdot D(E)\ dE}\right)\right) \\ &= \frac{1}{t}\left(-\log\left(\int_{E=0}^{E_{\max}} W(E)\ \mathrm{e}^{-\mu(\mathrm{E})\cdot \mathrm{t}}\,dE\right)\right)\end{aligned} \tag{3}$$

with the weighting function

$$W(E) = \frac{S(E)\cdot D(E)}{\int_{E=0}^{E_{\max}} S(E)\cdot D(E)\,dE}\,. \tag{4}$$

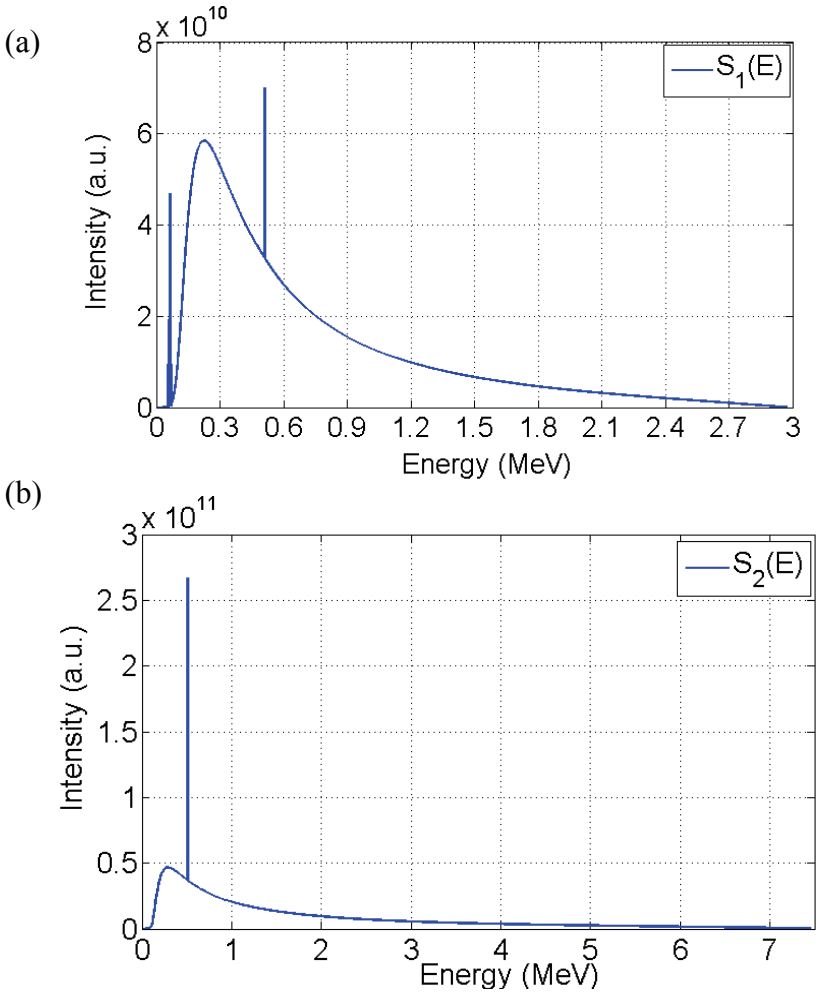

Fig. 1. Poly-energetic betatron X-ray spectra for source potential (a) 3 MV with 4 mm thick Cu pre-filter and (b) 7.5 MV with 10 mm thick Cu pre-filter, both simulated using aRTist software.

The poly-energetic X-ray spectra for the lower (3 MV) and the higher acceleration potential (7.5 MV), simulated using *aRTist* [11-13], are shown in Fig. 1.

2.1.1 Thickness-Independent Dual-Energy Function

For shorter paths of the X-rays (i.e. penetration through smaller objects), the effective total linear attenuation coefficient is approximated by [10] as

$$\mu_{eff} = \int_{E=0}^{E_{\max}} W(E)\,\mu(\mathrm{E})\,dE \quad . \tag{5}$$

For dual-energy measurements at conventional energies, the ratio of the effective linear attenuation coefficients for the low-energy spectrum μ_{Low} and for the high-energy spectrum μ_{High} can be then obtained by

$$\mathrm{F(Z)} = \frac{\mu_{Low}(Z)}{\mu_{High}(Z)} = \left(\frac{\int_{E=0}^{E_{\max Low}} W(E)\,\mu(\mathrm{E},Z)\,dE}{\int_{E=0}^{E_{\max High}} W(E)\,\mu(\mathrm{E},Z)\,dE} \right) \tag{6}$$

where F(Z) is called the dual-energy function.

2.1.2 Thickness-Dependent Dual-Energy Function

Generally, in the case of inspecting large cargo containers, the X-ray beam penetrates through dense objects and takes longer ray paths (on the order of meters). Consequently, the dual-energy function F(Z,t) not only depends on the material's atomic number Z, but also on the material thickness.

For dual high-energy measurements, the ratio of the effective linear attenuation coefficients for the low-energy spectrum μ_{Low} and for the high-energy spectrum μ_{High} can be obtained from the following modified formula

$$\mathrm{F}(\mathrm{Z},\mathrm{t}) = \frac{\mu_{Low}(\mathrm{Z},\mathrm{t})}{\mu_{High}(\mathrm{Z},\mathrm{t})} = \left(\frac{\log\left(\int_{E=0}^{E_{\max Low}} W(E)\, \mathrm{e}^{-\mu(\mathrm{E},\mathrm{Z})\cdot\mathrm{t}}\, dE \right)}{\log\left(\int_{E=0}^{E_{\max High}} W(E)\, \mathrm{e}^{-\mu(\mathrm{E},\mathrm{Z})\cdot\mathrm{t}}\, dE \right)} \right). \tag{7}$$

The above dual-energy function is explicitly dependent on the thickness t of the object being inspected.

Fig. 2 shows the dependence of the dual-energy function on the atomic number Z at high X-ray energies. The low-energy and high-energy X-ray spectra (see Fig. 1) together with the ideal dose-proportional detector response $D(E) = E$ are used in the numerical calculations for simplification purposes. The behavior of the thickness-independent dual-energy function F(Z), as shown in Fig. 2(a), is divided into two regions. Region 1 corresponds to low-Z materials (Z≤12) where most of the dangerous materials appear. F(Z) is nearly constant in this region. Hence, material discrimination is not possible between low-Z materials. On the other hand, F(Z) varies monotonically with Z in region 2 (i.e. Z>12), so a material discrimination is possible in this region. Furthermore, a sharp dip can be seen near Z=73 (tantalum) because the low-energy spectrum includes features characteristic for this material, as it is used for the target in the betatron X-ray source (see characteristic line of tantalum in Fig. 1(a)). Fig. 2(b) shows the thickness-dependent dual-energy function according to Eq. 7. A strong dependence of the dual-energy function on the thickness rather than the atomic number can be observed in Fig. 2(b). Thus, for dual high-energy X-ray imaging, the dependence of μ_{eff} on the material thickness has to be considered in order to improve the material discrimination capability.

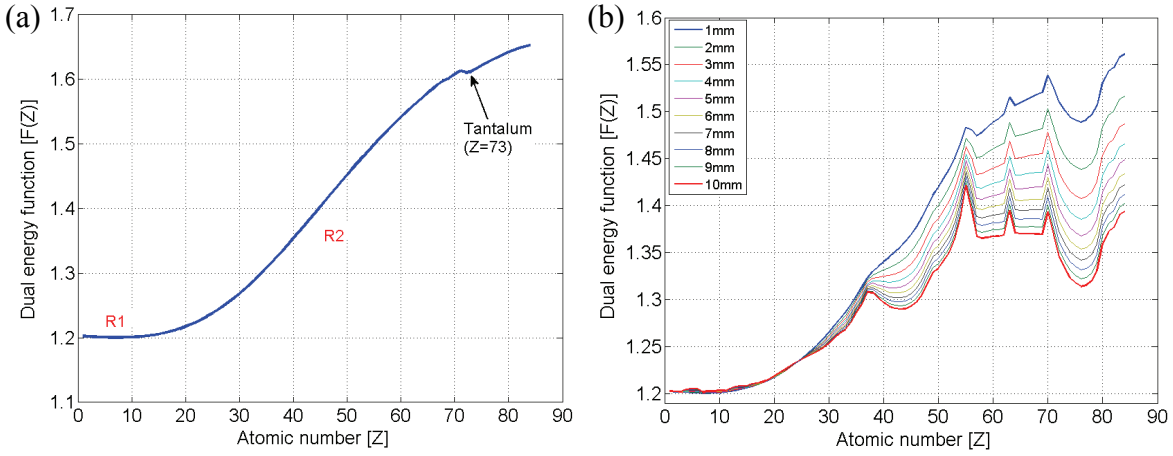

Fig. 2. Variation of dual-energy function with atomic number: (a) thickness-independent and (b) thickness-dependent dual-energy function. The selected low- and high-energy spectra correspond to 3 MV and 7.5 MV, respectively. These plots were calculated using an ideal dose-proportional detector response.

2.2 With Scattered Radiation

Generally, there is no analytical solution for evaluating the scatter effects in complex geometries and inhomogeneous materials. In this study, the influence of the scattered radiation on the dual-energy function is evaluated using the Monte Carlo code *McRay* which is an integrated solution in the radiographic simulator *aRTist* [14]. Using *aRTist-McRay* the interaction of photons with material (for both transmission and backscatter arrangements) can be calculated, while allowing the separation of primary and scattered contribution to the total intensity.

Fig. 3 shows the simulation setup for calculating the scattered radiation for a step wedge using *aRTist-McRay*. In order to analyze the dual-energy function for high-Z materials, an Sn (tin) step wedge with a thickness range between 1 mm and 10 mm with steps of 1 mm is used. The source-to-detector distance (SDD) and source-to-object distance (SOD) are 2.4 m and 2.15 m, respectively. For simplicity, an ideal dose-proportional detector is assumed in the Monte Carlo calculations. The detector size is 512×512 pixels. The number of traced photons for the Monte Carlo calculation is 1e12. The obtained dual-energy functions at each step with and without scattered radiation are shown in Fig. 4. Quantitatively, a change of about 5% due to the scatter contribution is observed at the 1 mm step. A reduction in the influence of scattered radiation with increasing thickness can be noticed in Fig. 4. In practical cargo inspection, it is important to more closely match the cargo container material and thickness in the image evaluation. In order to better resemble the cargo inspection, a 6 mm thick steel plate was placed between the Sn step wedge and the detector. The variation of the dual-energy function for the Sn step wedge considering the steel plate is shown in Fig. 5. As can be seen in Fig. 5, the thickness-dependence of the dual-energy function can be neglected in this case.

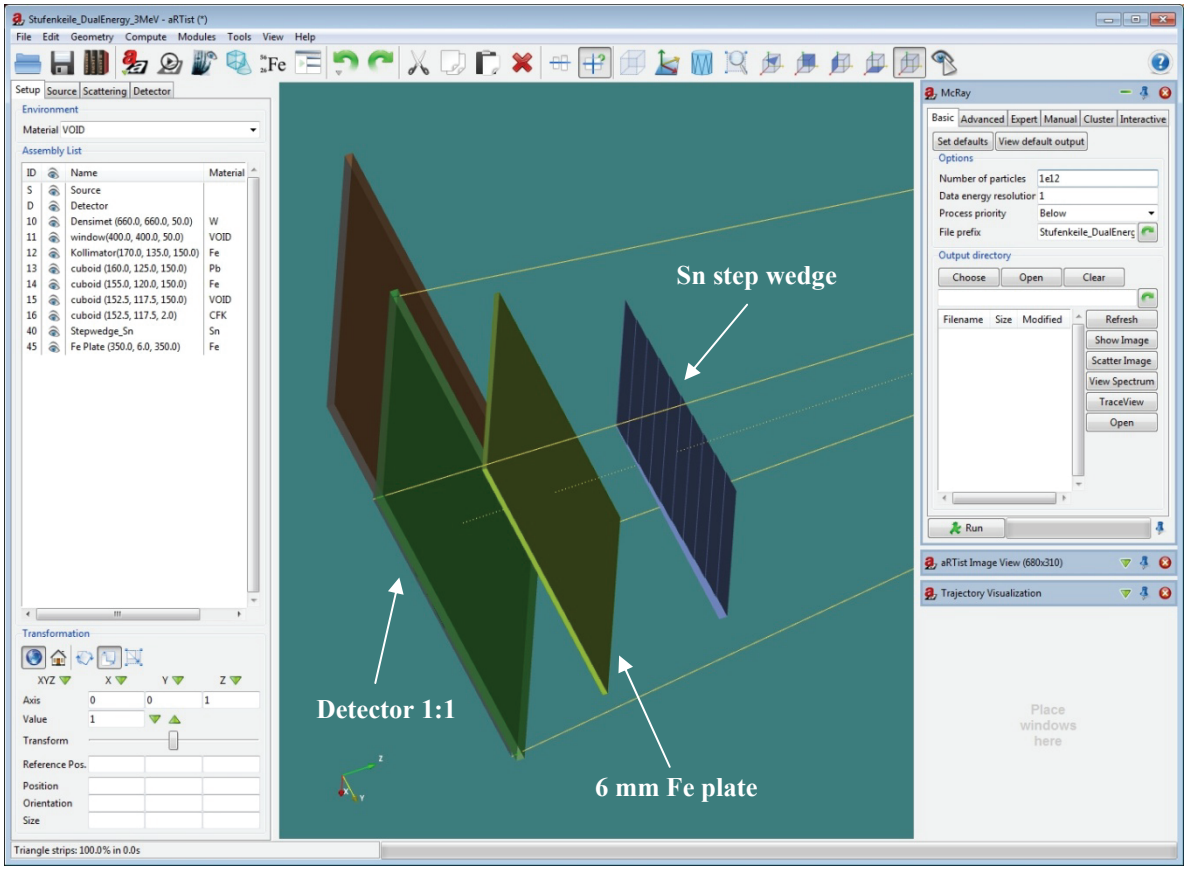

Fig. 3. Quantitative simulation of scatter effects on the dual-energy function using *aRTist-McRay*.

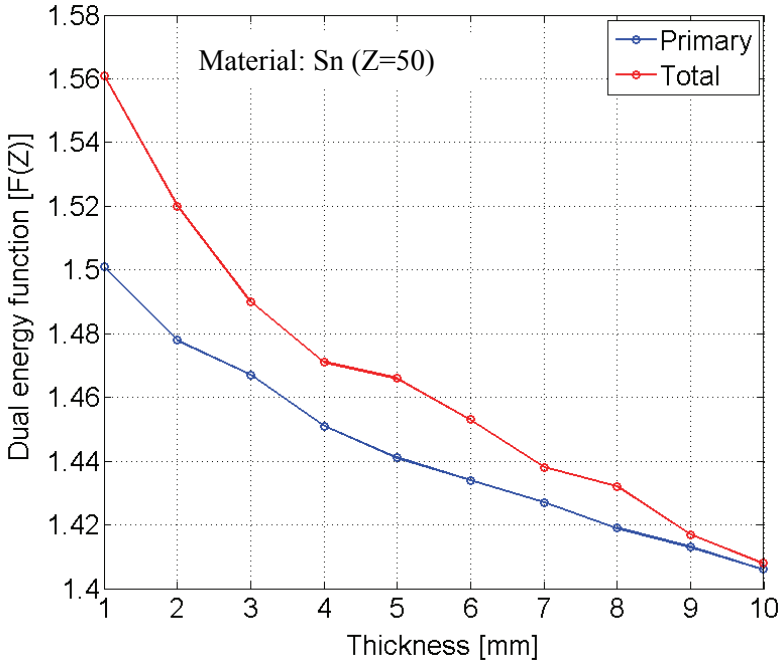

Fig. 4. Variation of dual-energy function with material thickness calculated using *aRTist-McRay*.

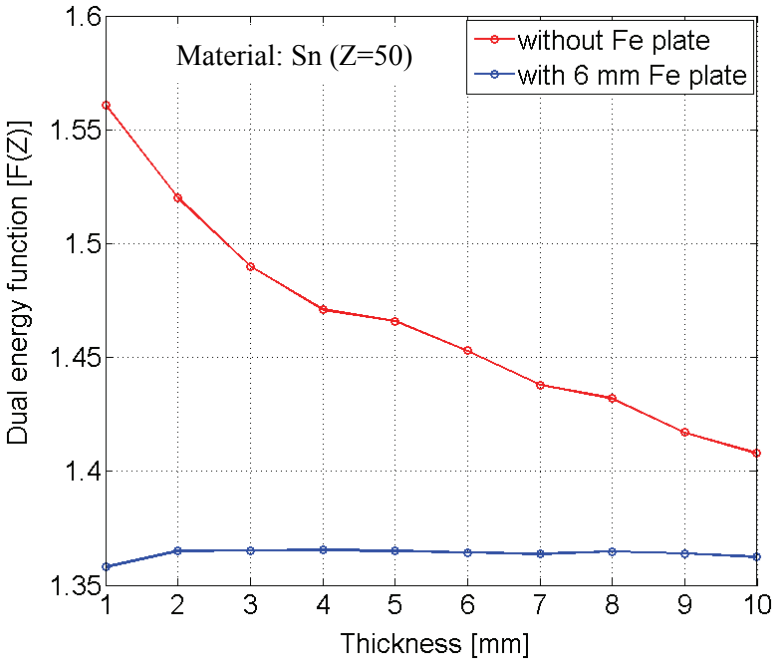

Fig. 5. Variation of dual-energy function with material thickness considering a 6 mm steel plate between the Sn step wedge and the detector.

3. Comparison with Experiments

3.1 Experimental Setup

In order to validate the simulation results described in section 2, dual-energy measurements have been performed at the high-energy X-ray laboratory at BAM. The experimental setup used for the dual-energy measurements is shown in Fig. 6. A pulsed betatron with 0.6 mm thick tantalum target was used to generate high-energy X-rays with a maximum energy of 7.5 MeV at a pulse repetition frequency of 200 Hz [15]. In this study, a high-resolution

DDA (Perkin Elmer XRD 1621) is used. The size of the detector is 40.96 cm×40.96 cm consisting of 2048×2048 pixels with a pixel size of 200 µm. The scintillating material is gadolinium oxysulfide (Gd_2O_2S, effective density 4.85 g/cm^3, thickness 0.436 mm). The developed test phantom is shown in Fig. 7 containing different low-Z (PMMA, Mg, Al) and high-Z (Fe, Cu, Sn) material step wedges. Additionally, a 6 mm thick steel plate is placed between the test phantom and the detector for simulating cargo container inspection. The detector sensitivity $D(E)$ is defined as the product of the probability of photon interaction and the average photon energy transfer per interaction for an incident photon of energy E. The energy-dependence of the detector sensitivity $D(E)$ has been calculated for the Gd_2O_2S scintillator shown in Fig. 8. For X-ray energies beyond 1 MeV the detector efficiency increases with increasing X-ray energy. On the other hand, the photon interaction probability decreases at higher X-ray energies.

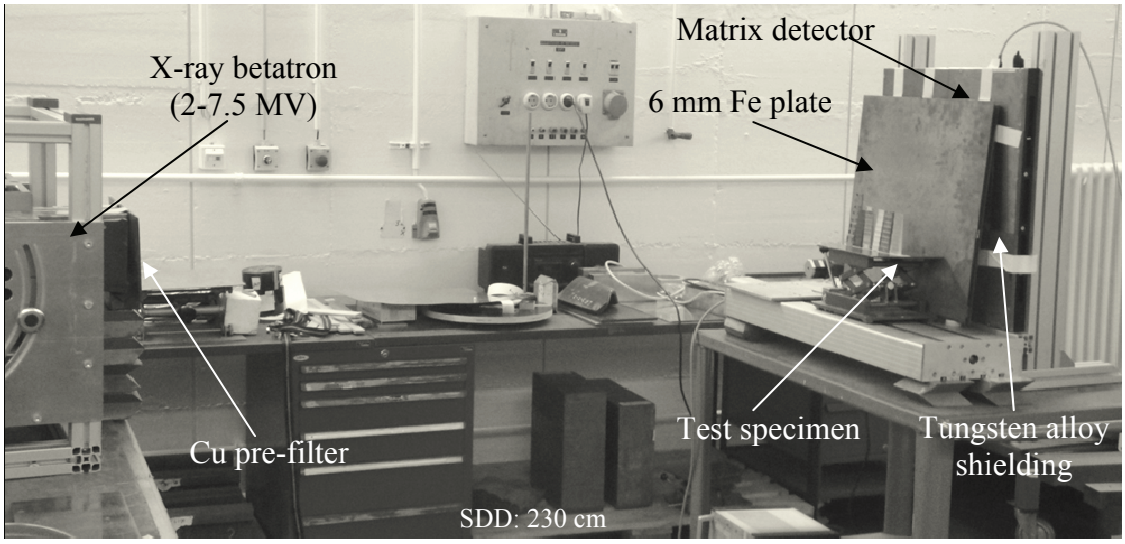

Fig. 6. Experimental setup used for dual high-energy X-ray measurements.

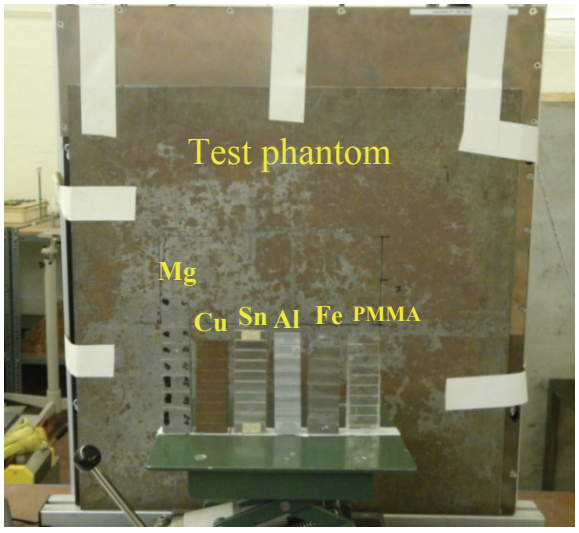

Fig. 7. Test phantom showing different low- and high-Z material step wedges.

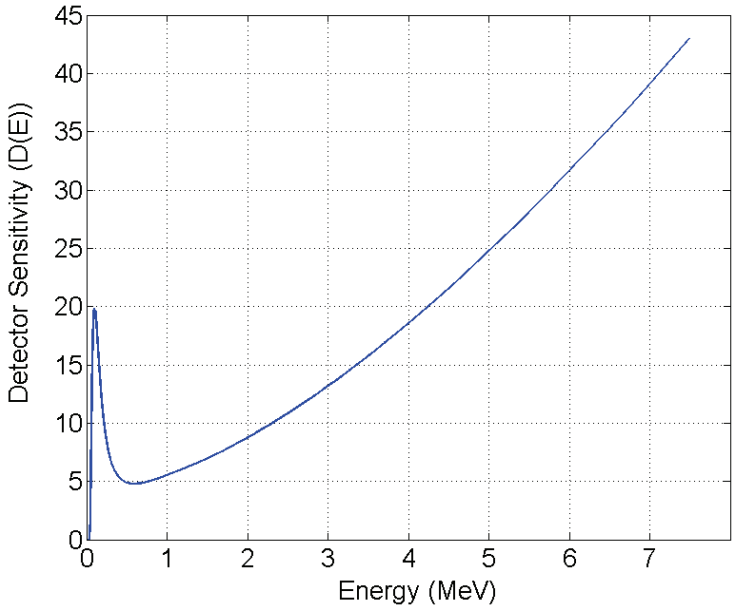

Fig. 8. Calculated detector efficiency $D(E)$ for the Gd_2O_2S scintillator used for the dual-energy measurements. The effective density and the thickness of the scintillator material are 4.85 g/cm^3 and 0.436 mm, respectively.

3.2 Comparison of the Results and Discussion

The dual-energy experiments are performed using 3 MV and 7.5 MV acceleration potentials of the betatron with pre filters of 4 mm and 10 mm Cu, respectively. The comparison between simulated and experimental dual-energy functions for the Sn step wedge is shown in Fig. 9. Here no steel plate is placed between the test specimen and the detector. A very good quantitative agreement between simulation and experiments can be seen in Fig. 9. For step thicknesses beyond 8 mm, a deviation of 1% is observed. The main reason for these minor discrepancies is a shift of the beam intensity maximum with acceleration potential of the betatron. This also leads to the mismatch in profile slope for these steps. Another reason may be the presence of undesired scattered radiation from surroundings (e.g. manipulator) in the case of experiments which is not considered in the simulation. For the high-energy method examined here, the probability of discriminating materials is reduced with increasing material thickness. In this case scattered radiation influences the material discrimination capability but still shows a thickness-dependence of the dual-energy function.

A comparison between simulated and experimental dual-energy functions for the Sn step wedge is shown in Fig. 10, placing a 6 mm steel plate between the specimen and the detector to more closely match the cargo inspection. As in the previous case, good agreement between the experimental results and the simulation has been found. For determining the effective linear attenuation coefficients μ_{Low} and μ_{High} the same incident intensities I_0 have been used as for the case without additional steel plate, because for cargo inspection only these values are accessible. The realistic experimental setup discussed here in this case also leads to a decrease of the dual-energy function with increasing material thickness, i.e. the thickness-dependence is not negligible. This is found in the experiments as well as in the simulation. Compared to the results without steel plate the single steps are less pronounced due to the additional scatter contribution from the steel plate.

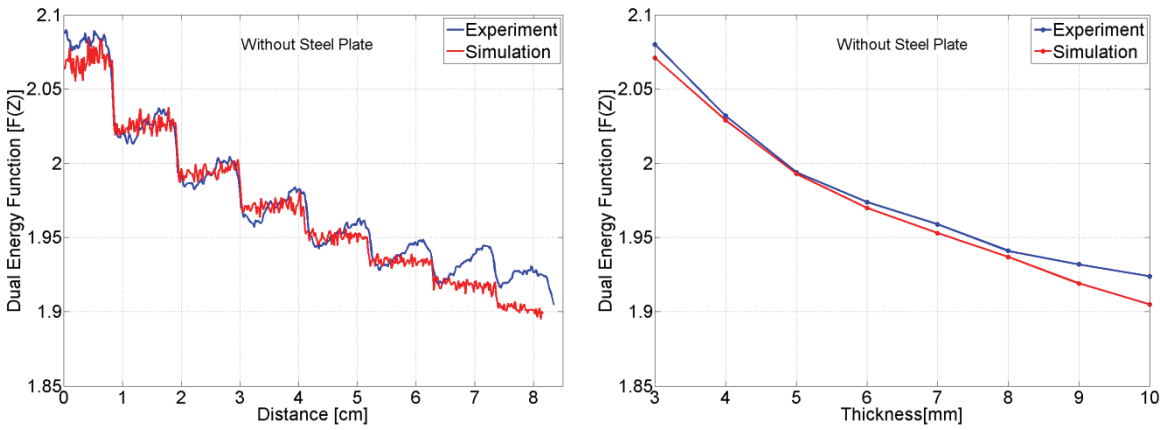

Fig. 9. Comparison of simulated and experimental dual-energy functions for the Sn step wedge (a) profiles and (b) variation of the dual-energy function with the material thickness.

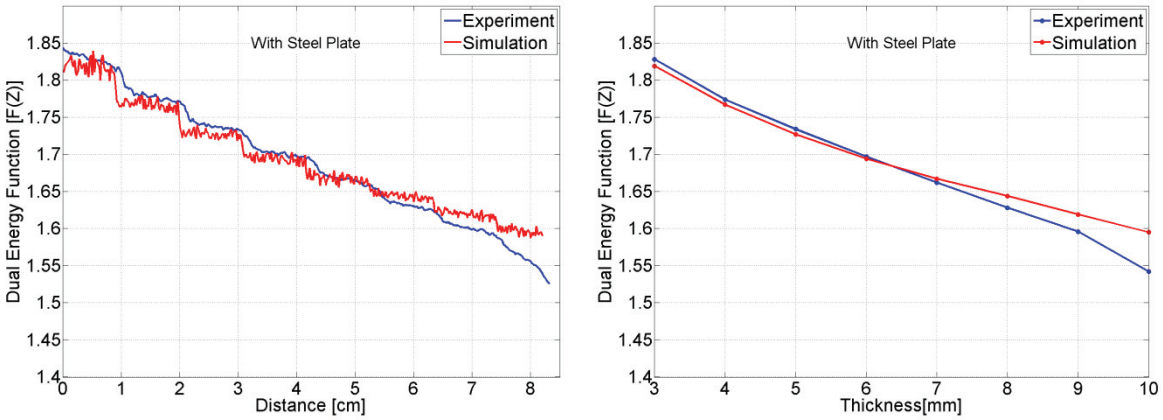

Fig. 10. Comparison of simulated and experimental dual-energy functions for the Sn step wedge (a) profiles and (b) variation of the dual-energy function with the material thickness for simulation of container inspection by placing a steel plate between specimen and detector.

3. Conclusions

In conclusion, the applicability of a dual high-energy X-ray imaging technique for material discrimination in cargo containers is evaluated. Numerical results on the variation of the dual-energy function with the atomic number Z at higher X-ray energies showed that the material discrimination capability is reduced for atomic numbers $Z \leq 10$ and $Z \geq 36$. It is also observed that the accuracy of the material discrimination in cargo containers could be improved by considering the effect of the material thickness on the effective attenuation coefficients. Dual-energy measurements were carried out using a portable high-energy (2-7.5 MeV) X-ray betatron and a digital detector array with high spatial resolution. The measured dual-energy functions for the test phantom containing low- and high-Z material step wedges were compared with the *aRTist-McRay* simulation results. A good quantitative agreement between simulation and experiments was achieved.

While a high-resolution digital detector array was used in the present dual-energy experiments, scattered radiation can be further minimized by employing line detectors, which detect only a finely collimated X-ray beam.

References

[1] R E Alvarez and A Macovski, 'Energy-selective reconstructions in X-ray computerized tomography', Phys. Med. Biol., Vol 21, pp 733-744, 1976.

[2] L Yu, X Liu, and C H McCollough, 'Pre-reconstruction three-material decomposition in dual-energy CT', Proceedings of SPIE, Medical Imaging, Vol 7258, 72583V, 2009.

[3] M Bastan, M R Yousefi, and T M Breuel, 'Visual words on baggage X-ray images', Computer Analysis of Images and Patterns, Lecture Notes in Computer Science, Vol 6854, pp 360-368, 2011.

[4] S Orogodnikov and V Petrunin, 'Processing of interlaced images in 4-10 MeV dual energy customs system for material recognition', Physical Review Special Topics - Accelerators and Beams, Vol 5, pp 104701-11, 2002.

[5] M Stein, V A Kasyanov, V A Chaklov, J Macleod, P Marjoribanks, and S Hubbard, 'Small size betatrons for radiographic inspection', Proceedings of 16th World Conference on Non-Destructive Testing (WCNDT), Radiography, Montreal, Canada, 2004.

[6] S Kolkoori, N Wrobel, K Osterloh, B Redmer, A Deresch, and U Ewert, 'High-Energy Radiography for Detecting Details in Highly Complex Packings', Materials Testing, Vol 55, No. 9, pp 683-688, 2013 (in German).

[7] U Ewert, U Zscherpel, K Heyne, M Jechow, and K Bavendiek, 'Image quality in digital industrial radiology', Materials Evaluation, Vol 70, No. 8, pp 955-964, 2012.

[8] U Ewert, U Zscherpel, and M Jechow, 'Essential parameters and conditions for optimum image quality in digital radiology', Proceedings of 18th World Conference on Nondestructive Testing (WCNDT), Durban, South Africa, 16-20 April, 2012.

[9] B J Heisemann, J Lippert, and K Stierstorfer, 'Density and atomic number measurements with spectral X-ray attenuation method', Journal of Applied Physics, Vol 94, No. 3, pp 2073-79, 2003.

[10] X Liu, L Yu, A Primak, and C. McCollough, 'Quantitaive imaging of element composition and mass fraction using dual-energy CT: Three-material decomposition', Medical Physics, Vol 36, pp 1602-9, 2009.

[11] G R Tillack, C Nockemann, and C Bellon, 'X-ray modelling for industrial applications', NDT&E International, Vol 33, pp 481–488, 2000.

[12] C Bellon and G R Jaenisch, 'aRTist –analytical RT inspection simulation tool', Proceedings of the International Symposium on Digital Industrial Radiology and Computed Tomography, Lyon, France, June 25-27, 2007.

[13] A Deresch, G R Jaenisch, C Bellon, and A Warrikhoff, 'Simulating X-ray Spectra: From Tube Parameters to Detector Output', Proceedings of 18th World Conference on Nondestructive Testing (WCNDT), Durban, South Africa, April 16-20, 2012.

[14] C Bellon, A Deresch, and G R Jaenisch, 'Radiography Simulation with aRTist – Combining and Analytical and Monte Carlo Methods', Proceedings of International Symposium on Digital Industrial Radiology and Computed Tomography, Ghent, Belgium, June 22-25, 2015.

[15] JME Portable 7.5 MeV X-ray Betatron for Radiographic Non-Destructive Testing, User Manual, Issue **1**, 2006.